Supporting Information

Tailoring Selenium Vacancies in $MoSe_2$ through Oxygen Passivation for Room-Temperature NO_2 Sensing Enhancement

Shengliang Zheng,[a] Dongmin Yin,[a] Shengpei Zhang,[a] You Wang ,*[a] Jiayu Li,[b] Zhengjia Wang*[c],

Ye Yuan,[d] Hsu-Sheng Tsai[e,f] and Juanyuan Hao*[a]

[a] *School of Materials Science and Engineering, Harbin Institute of Technology, Harbin 150001, P. R. China.*
[b] *State Key Laboratory of Inorganic Synthesis and Preparative Chemistry, College of Chemistry, Jilin University, Changchun 130012, China.*
[c] *School of Instrumentation Science and Engineering, Harbin Institute of Technology, Harbin 150001, P. R. China.*
[d] *Songshan Lake Materials Laboratory, Dongguan, Guangdong 523808, P. R. China.*
[e] *Laboratory for Space Environment and Physical Sciences, Harbin Institute of Technology, Harbin 150001, P. R. China.*
[f] *School of Physics, Harbin Institute of Technology, Harbin 150001, P. R. China.*

Corresponding authors E-mail: y-wang@hit.edu.cn; zhengjiawang@hit.edu.cn; jyhao@hit.edu.cn;

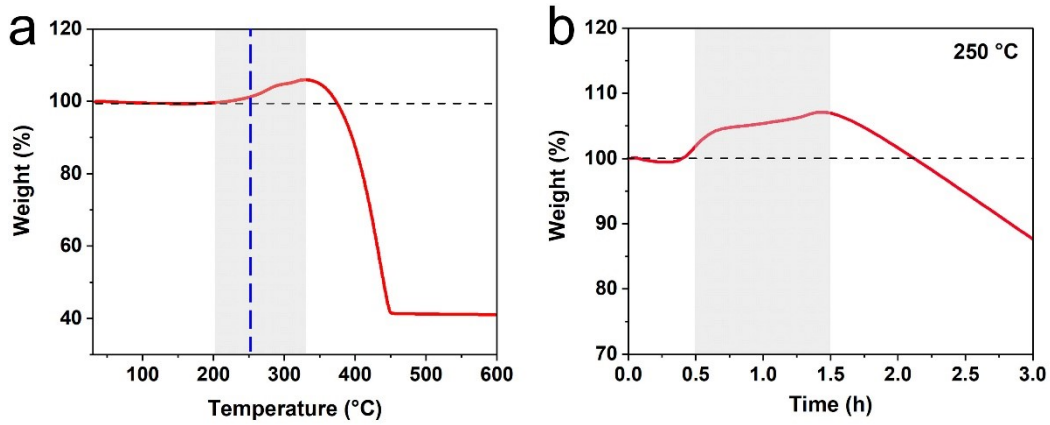

Fig. S1. TGA curves of $MoSe_2$-SeV (a) record in the temperature from 30 to 600 °C with a heating rate of 10 °C/min, and (b) record at 250 °C for 3 h. According to the TGA curve in Fig. S1a, the annealing temperature was determined to be 250 °C, at which the weight of $MoSe_2$-SeV is increased slowly possibly due to the embed of oxygen atoms at Se vacancy sites. The relatively low annealing temperature would facilitate the following precise control of annealing time. As for the annealing time, the weight of $MoSe_2$-SeV increases within 1.5 h at 250 °C in Fig. S1b, therefore the times of 0.5 to 1.5 h were chosen to tailoring the vacancy density of $MoSe_2$-SeV. Higher temperatures and longer annealing time will result in a loss of the material weight due to the gasification of SeO_2 during the oxidation of $MoSe_2$.

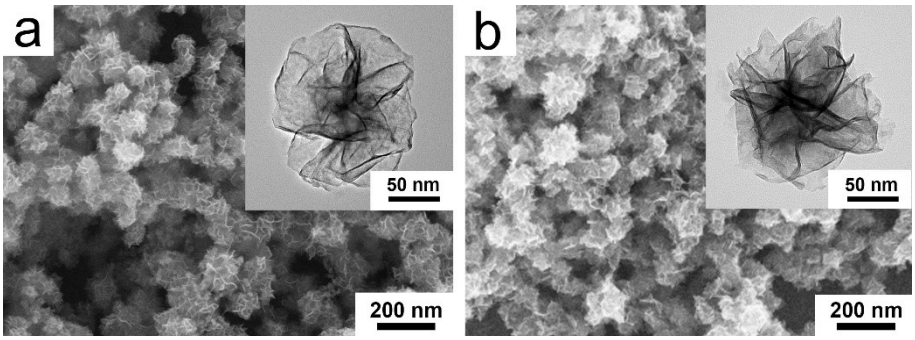

Fig. S2. SEM and HRTEM (insets) images of (a) $MoSe_2$-SeVO1, and (b) $MoSe_2$-SeVO3 nanoflowers. The nanoflower morphology of $MoSe_2$-SeV remains intact after annealing for 0.5 and 1.5 h.

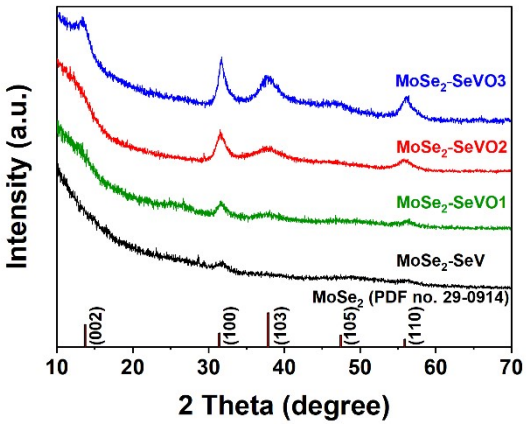

Fig. S3. XRD patterns of the $MoSe_2$-SeV, $MoSe_2$-SeVO1, $MoSe_2$-SeVO2, and $MoSe_2$-SeVO3. The crystal structures of $MoSe_2$-SeV are assigned to the hexagonal 2H-$MoSe_2$ phase ((PDF no. 29-0914) before and after oxygen passivation, and the crystalline degree is increased with the annealing time which can be ascribed to the decrease of SeV density brought by oxygen passivation.

Table S1. The Raman A_{1g} peak frequencys, the corresponding Se vacancy contents, and the percentages of Se vacancies filled up by O of each sample.

Samples	A_{1g} frequency (cm^{-1})	SeV content	O filled SeV
$MoSe_2$-SeV	229	21%	--
$MoSe_2$-SeVO1	232	16%	5%
$MoSe_2$-SeVO2	233	13%	8%
$MoSe_2$-SeVO3	235	10%	11%

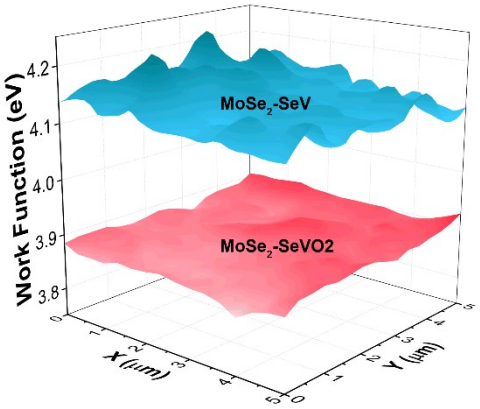

Fig. S4. Work function maps of $MoSe_2$-SeV and $MoSe_2$-SeVO2 measured by KPFM. The observed smaller work function of $MoSe_2$-SeVO2 (3.87 eV) than that of $MoSe_2$-SeV (4.15 eV) manifests the higher electron density of $MoSe_2$-SeVO2 after oxygen passivation.

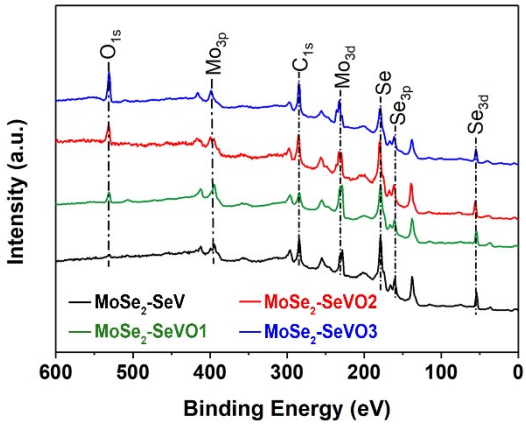

Fig. S5. XPS survey of the $MoSe_2$-SeV, $MoSe_2$-SeVO1, $MoSe_2$-SeVO2, and $MoSe_2$-SeVO3. The intensity of O 1s increases with the annealing time, indicating the oxygen element content of $MoSe_2$ increases through oxygen passivation.

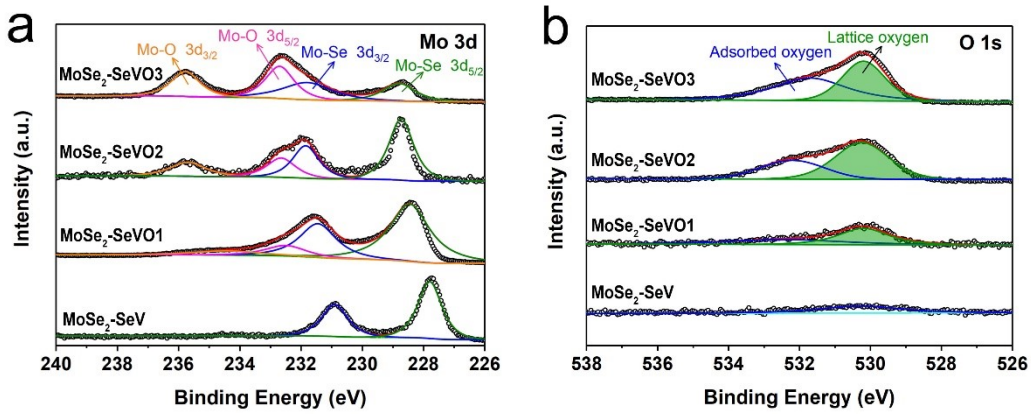

Fig. S6. (a) Mo 3d and (b) O 1s XPS spectra of the $MoSe_2$-SeV, $MoSe_2$-SeVO1, $MoSe_2$-SeVO2, and $MoSe_2$-SeVO3. The contents of Mo–O bond and lattice oxygen increase with the annealing time.

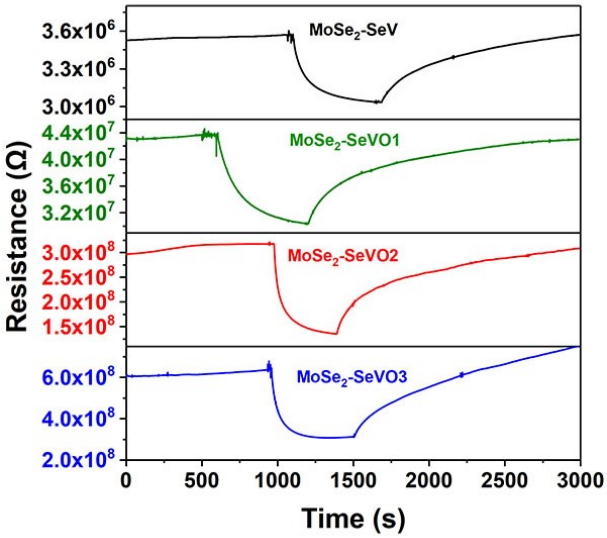

Fig. S7. The real-time resistance curves of the $MoSe_2$-SeV, $MoSe_2$-SeVO1, $MoSe_2$-SeVO2, and $MoSe_2$-SeVO3 towards 1 ppm NO_2 at room temperature.

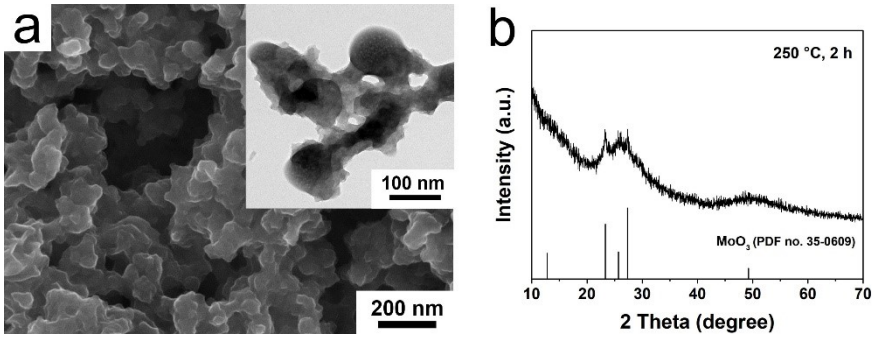

Fig. S8. (a) SEM and TEM (inset) images and (b) XRD pattern of the $MoSe_2$-SeV annealed at 250 °C for 2 h. The heterostructure of $MoSe_2$-SeV nanoflower collapses and the becomes to MoO_3 (PDF no. 35-0609), indicating the surface of the $MoSe_2$ starts to be oxidized and the lattice structure gradually changes to MoO_3.

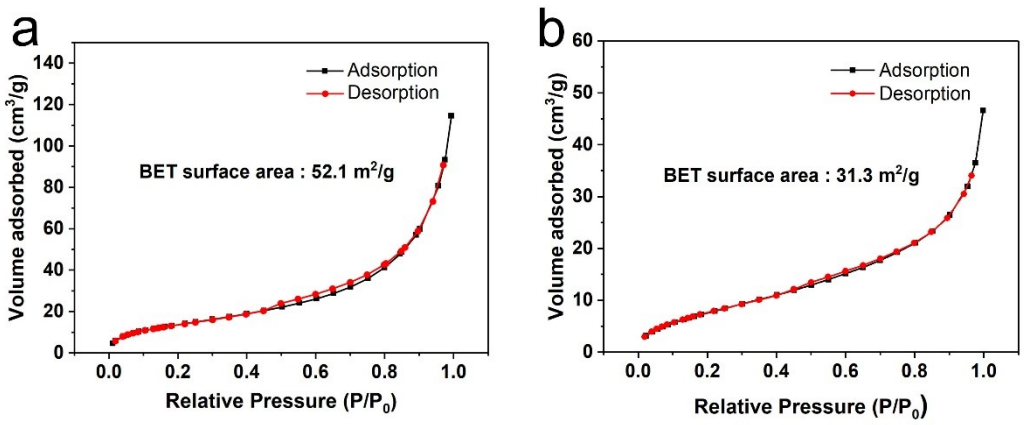

Fig. S9. The nitrogen adsorption and desorption isotherms of (a) $MoSe_2$ nanoflower, and (b) collapsed $MoSe_2$ nanoflower after 2 h annealing.

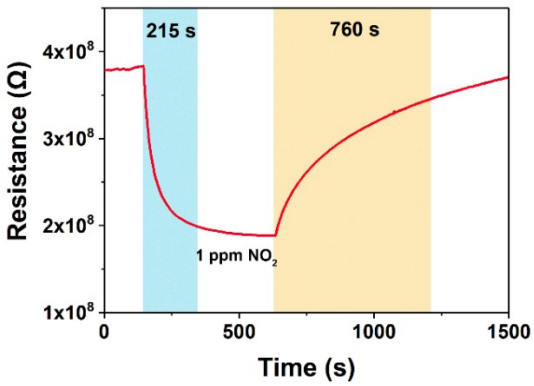

Fig. S10. The response and recovery curve of the $MoSe_2$-SeVO2 sensor towards 1 ppm NO_2, from which the response/recovery time of $MoSe_2$-SeVO2 is calculated to be 215/760 s.

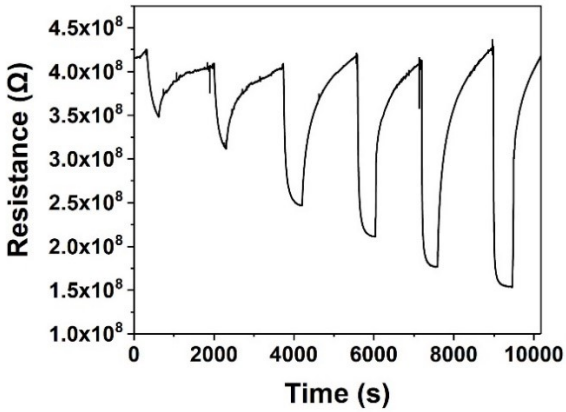

Fig. S11. The corresponding real-time resistance curve from the dynamic response test in the sensing studies.

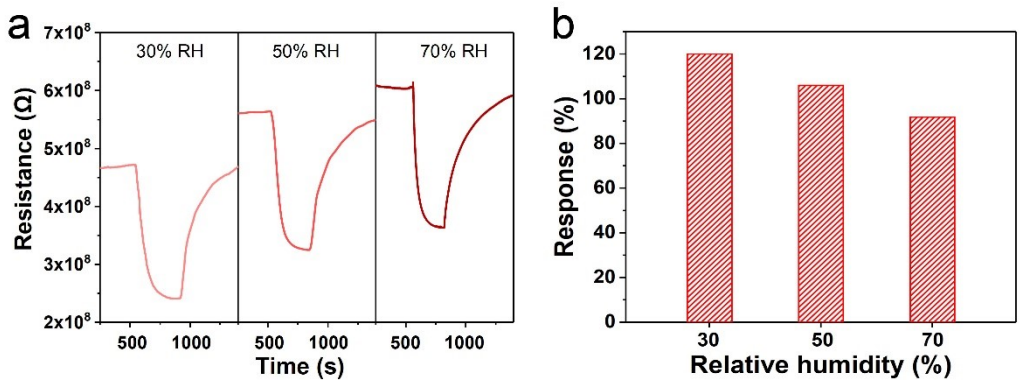

Fig. S12. The sensing (a) resistance curves and (b) response of the $MoSe_2$-SeVO2 sensor to 1 ppm NO_2 at room temperature. The higher baseline resistance of the $MoSe_2$-SeVO2 sensor in higher humidity could be explained by the interaction between the water molecule (as electron donor) and the $MoSe_2$-SeVO2 (p-type electron acceptor).

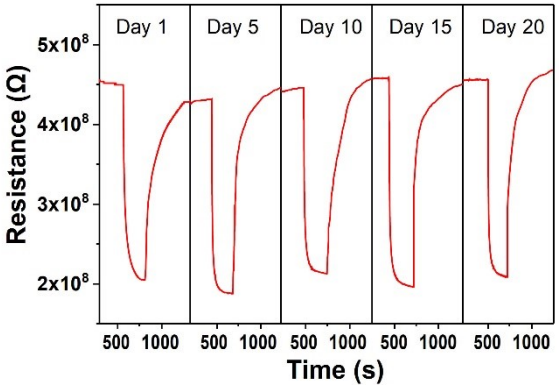

Fig. S13. The real-time resistance curves of the $MoSe_2$-SeVO2 sensor towards 1 ppm NO_2 at room temperature during stability test of for 20 days.

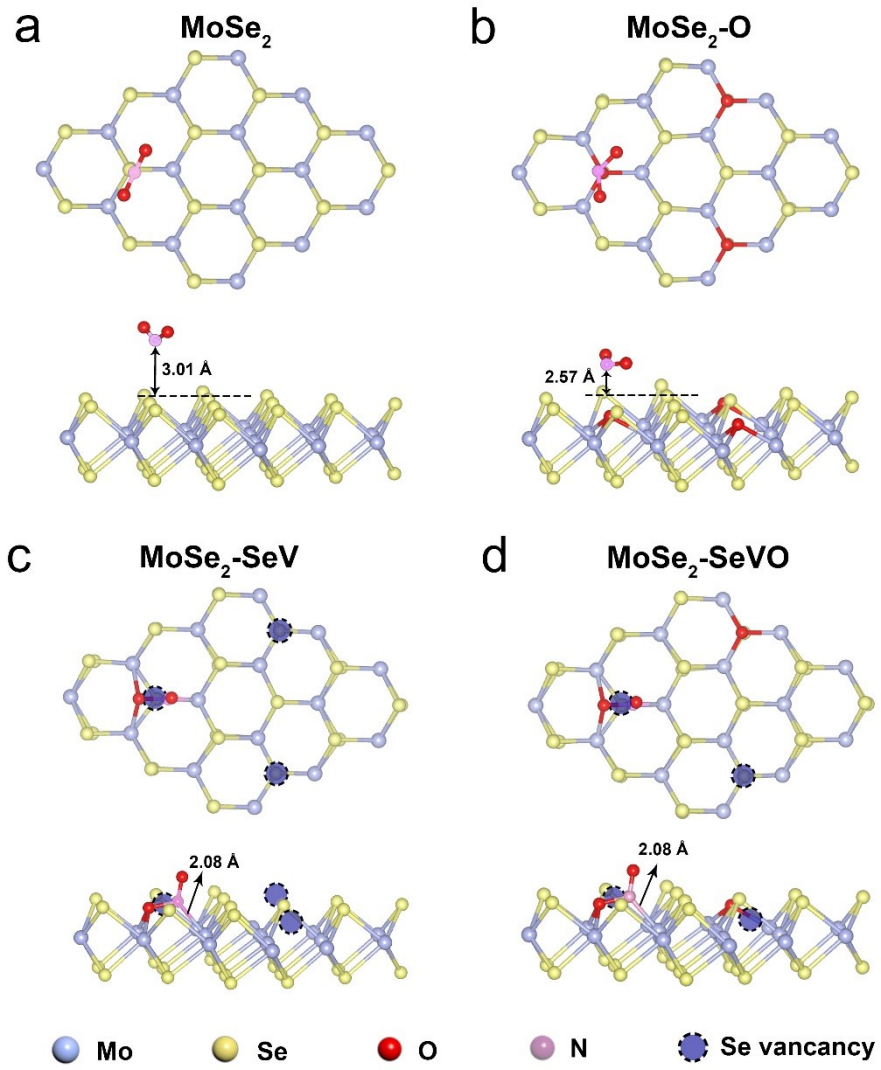

Fig. S14. Top and side views of the most stable adsorption configurations of NO_2 on (a) $MoSe_2$, (b) $MoSe_2$-SeV, (c) $MoSe_2$-SeVO, and (d) $MoSe_2$-O.

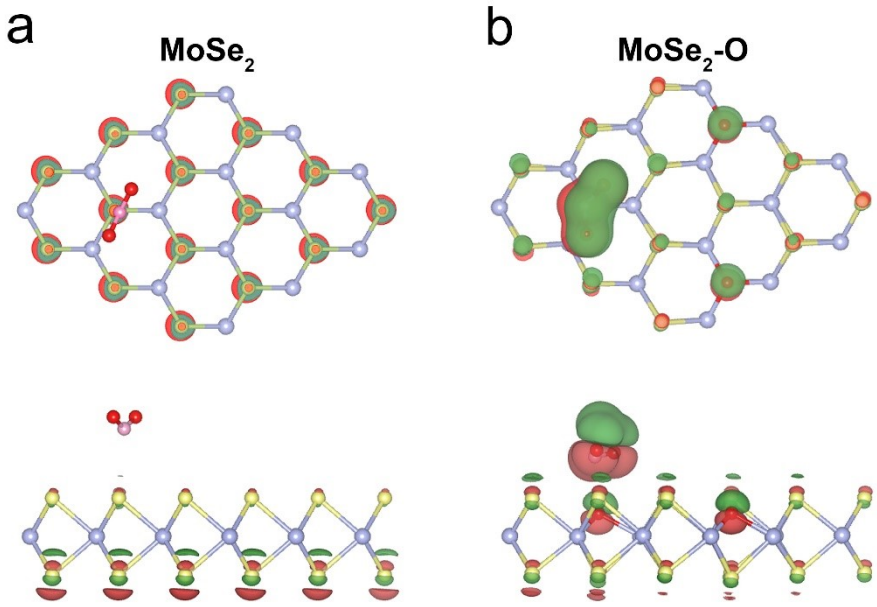

Fig. S15. The top and side views of the charge density difference (CDD) plots for adsorbed NO_2 on (a) $MoSe_2$ and (b) $MoSe_2$-O. Red/green regions represent the areas of electron accumulation/depletion. The isosurface value is 0.18 e $Bohr^{-3}$.